

Manuscript version: Author's Accepted Manuscript

The version presented in WRAP is the author's accepted manuscript and may differ from the published version or Version of Record.

Persistent WRAP URL:

<http://wrap.warwick.ac.uk/119334>

How to cite:

Please refer to published version for the most recent bibliographic citation information. If a published version is known of, the repository item page linked to above, will contain details on accessing it.

Copyright and reuse:

The Warwick Research Archive Portal (WRAP) makes this work by researchers of the University of Warwick available open access under the following conditions.

© 2019 Elsevier. Licensed under the Creative Commons Attribution-NonCommercial-NoDerivatives 4.0 International <http://creativecommons.org/licenses/by-nc-nd/4.0/>.



Publisher's statement:

Please refer to the repository item page, publisher's statement section, for further information.

For more information, please contact the WRAP Team at: wrap@warwick.ac.uk.

Development of a XYZ Scanner for Home-made Atomic Force Microscope Based on FPAA Control

Yanling Tian^{1,2*}, Kunhai Cai^{1,2}, Dawei Zhang¹, Xianping Liu², Fujun Wang¹, Bijan Shirinzadeh³

¹Key Laboratory of Mechanism Theory and Equipment Design of Ministry of Education, Tianjin University, Tianjin 300072, China

²School of Engineering, University of Warwick, Coventry CV4 7AL, UK

³Robotics and Mechatronics Research Laboratory, Department of Mechanical and Aerospace Engineering, Monash University, Clayton, VIC 3800, Australia

Abstract: Atomic force microscopy (AFM) is one of the useful tools in the fields of nanoscale measurement and manipulation. High speed scanning is one of the crucial requirements for live cell imaging and soft matter characterization. The scanning speed is limited by the bandwidth of the AFM's detection and actuation components. Generally, the bandwidth of a traditional scanner is too low to conduct the live cell imaging. This paper presents a simple and integrated compact home-made AFM for high speed imaging. To improve the bandwidth of the scanner, a parallel kinematics mechanism driven by piezoelectric actuators (PZTs) is proposed for the fast positioning in the X, Y and Z directions. The mechanical design optimization, modeling and analysis, and experimental testing have been conducted to validate the performance of the proposed scanner. A number of experimental results showed that the developed scanner has the capability for broad bandwidth with low coupling errors in the actuation directions. A hybrid control strategy including feedforward and feedback loops has been designed to significantly improve the dynamic tracking performance of the scanner and a field programmable analog array (FPAA) system is utilized to implement the control algorithm for excellent and stable tracking capability. Further, a number of high speed measurements have been conducted to verify the performance of the developed AFM.

Keywords: XYZ scanner, Field programmable analog array, Home-made AFM, High speed scanning

1. Introduction

Atomic force microscopy (AFM) is one of the powerful and widely used tools in the fields of nanoscale imaging, measurement, manipulation, and manufacturing [1-3]. In general, an AFM consists of sensing and actuation components including the cantilever with a sharp tip, the scanner, the detection laser, the position sensitive photodiode (PSD), and the signal processing control system. During scanning process, the cantilever will bend and deflect the laser beam on the PSD. In contact mode scanning, the deflection of the cantilever or the force between tip and sample remains constant through a feedback control scheme. The topographical information of the sample can be derived from the command signal generated by the controller to actuate the z axis of the scanner. The contact mode scanning has been widely utilized to obtain high-resolution images of protein, blood cells and other biological systems [4, 5]. Based on the contact mode AFM and conductive probe, the mechanical and electrical properties of a number of functional materials including electroactive polymers, biomolecules, and piezoelectric crystals can be measured [6]. Further, understanding the electrical and electromechanical characteristics at the nanoscale is one of the important requirements for semiconductor material design [7, 8]. However, traditional AFM generally suffers from the limitation of slow imaging rate due to the low bandwidth of the scanning process. This indicates that it is a time-consuming task to conduct AFM imaging. For example, a commercial AFM would take at least 2 minutes to obtain a 128×128 pixels resolution image with a typical scan rate of 1 Hz [9], which is too slow for the imaging and investigating of biological processes [10, 11] and nanofabrication [12, 13]. In order to broaden the scope of AFM applications, high speed scanning and imaging is required for both academic and industrial researchers. The scanning speed is typically constrained by four factors, including the

resonance frequencies of cantilever and scanner, the bandwidth of controller and the data processing system [14].

To overcome the previously mentioned shortcomings, small-sized, high bandwidth [15, 16] and low quality factor (Q factor) [17] cantilevers were proposed to improve the imaging sensitivity and speed. As one of the other key components, the scanner has a significant impact on the imaging speed. Conventionally, piezoelectric tube is one of the most widely utilized scanners in commercial AFMs. It has excellent resolution, compact structure, easy to install and configure. However, it has two fatal flaws including low resonance frequency and cross coupling errors, which significantly affect the scanning rate and reduce the imaging quality. There are two techniques which are proposed to address the above issues. One is to utilize a new spiral scanning trajectory, instead of the raster scanning [18]. However, a suitable and even complex control algorithm must be developed to accurately track the spiral scanning trajectory. This will inevitably increase the complexity of the scanning, and also requires a high performance controller. The other seeks to establish an alternative scanner, which has high resonance frequency and motion accuracy, to replace the piezoelectric tube. Recent research efforts have been directed towards the flexible hinge based scanners. Leang and Fleming [19] presented a 2-axis (XY) high-speed scanner. Wadikhaye et al. [20] proposed a high-speed serial-kinematic XY nanopositioner. A compact XYZ scanner for high-speed atomic force microscopy was also developed and reported [21, 22]. Another high-performance XYZ scanner was integrated with a commercial scan-by-probe AFM [23]. All these scanners are based on serial-kinematics mechanism. Utilizing the parallel kinematics mechanism, efficient and high-bandwidth scanners were developed by Schitteret [24], Li [25] and Yong [9]. Since parallel kinematics mechanisms offer high motion accuracy, large mechanical stiffness, high resonance frequencies and compactness, they are increasingly utilized in high-speed nano-positioning applications.

The bandwidth of the sensing and control system also affects the imaging speed. Currently, most of the AFMs use digital signal processing (DSP) and feedback controllers. In such digital systems, the signals need to be sampled and afterwards

quantized by analog-to-digital (A/D) converter prior to sending the required data to DSP. Similarly, the command signals also need to be converted into the analog outputs to drive the actuators. These conversion and quantization processes will introduce delays and errors, and thus decrease the scanning speed. In order to achieve high speed, low noise and high accuracy, improved ADCs, DACs and DSPs are required. These initiatives easily lead to increased costs, power consumption, system size and complexity. Even field programmable gate arrays (FPGA) based digital controllers suffer from the similar problems. Over the past few years, field programmable analog array (FPAA) controllers have been used to successfully control various physical processes [26-28]. Based on switched capacitor technology, FPAA is an integrated circuit and uses configurable analog blocks for implementing various analog functions. The interconnected network can be programmed using on-chip memories. For instance, an Anadigm[®] FPAA QUADAPEX development board [29] allows to process and control complex analog signals and functions, and it can provide broad bandwidth, and thus eliminate/reduce the shortcomings of the digital processors.

This paper proposes a high-speed flexure-based XYZ scanner driven by piezoelectric actuators. The mechanical design optimization has been conducted to obtain high resonance frequencies and low cross-coupling effects in the actuation directions. The developed scanner consists of a parallel kinematics XY stage and a Z stage mounted on the central moving platform of the XY stage. Detailed parameter design and analysis have been performed to improve static and dynamic performance of the scanner. Finite element analysis (FEA) was utilized to validate the theoretical modeling and computational results. The prototype of the scanner has been constructed based on optimized results, and a number of experimental studies conducted to validate the established models and the performance of the developed scanner. In order to improve the tracking accuracy of the scanner, a feedforward/feedback hybrid control strategy has been proposed to eliminate/reduce the hysteresis of PZTs. FPAA was used to implement the control algorithms. Based on the developed scanner and FPAA controller, a compact, miniaturized and

integrated home-made AFM has been proposed. Using hybrid control strategies, high speed scanning has been conducted to measure the surface topography of standard grating. It is noted that the home-made AFM has the capability for high speed imaging and characterisation.

The remainder of this paper is organized as follows. Section 2 introduces the mechanical design of XYZ scanner. Section 3 provides the model verification and prototype development. In Section 4, a control scheme is proposed and implemented for the scanner, in order to improve tracking performance. A home-made AFM is developed and high speed imaging is performed in Section 5. Conclusions are provided in Section 6.

2. Mechanical design

2.1 Conceptual design

The conceptual design of the XYZ scanner is conducted to obtain high resonance frequencies and low cross-coupling errors between actuation directions. Based on a hybrid kinematics mechanism, the scanner mainly consists of a planar parallel XY stage and a vertical Z stage which is serially mounted on the moving platform of the XY stage. Three PZTs are utilized to drive the flexure based mechanism as shown in Fig. 1. In order to eliminate/reduce the mutual influences in the X and Y directions, two identical flexure based kinematic chains are arranged in the X and Y axes, and thus guarantee uniform characteristics of the moving platform. The schematic diagram of the decoupled XY stage is shown in Fig. 2(a). The moving platform is connected to four linkages through four parallel flexure mechanisms (three leaf-spring hinge), and the four linkages are connected to the frame through another eight parallel flexure mechanisms (two leaf-spring hinge). The Z stage (as shown in Fig. 2(b)) can be mounted on the moving platform with four bolts. The moving part of the Z stage is connected to the frame through four leaf-spring hinges with a separation angle of 90° . Thus the moving part of Z stage can move vertically without cross-coupling with other axes. Due to the hybrid kinematics mechanism, the moving part of the proposed stage can move in the X, Y and Z directions for the application of AFM scanning.

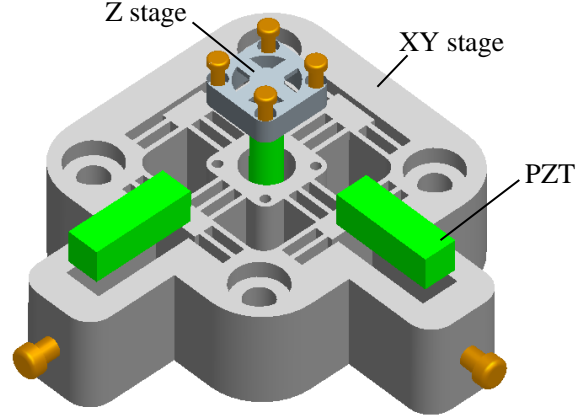


Figure 1. Exploded view of the proposed scanner

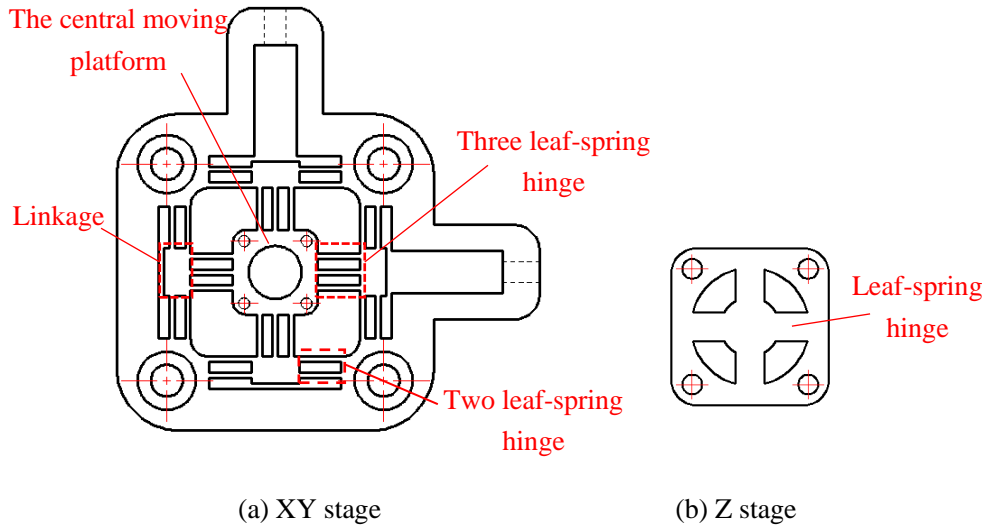


Figure 2. Schematic diagram of the flexure-based scanner

2.2 Theoretical modelling and analysis

In order to maintain the contact state and avoid separation between the PZTs and the flexure mechanism during positioning tasks, preloads for the PZTs are applied and adjusted through fine preloading screw. For simplicity and without loss of generality, only the kinematics chain in the Y direction is considered. As shown in Fig. 3(a), the PZT contacts with the parallel flexure mechanisms through the preload F_{pre} . From dynamics point of view, the model of the piezo-driven flexure mechanism can be considered as a damped mass and spring system and shown in Fig. 3(b), where k_{pzt} is the stiffness of PZT, k_c is the equivalent contact stiffness, and K_y is the equivalent stiffness in the Y direction of scanner. Due to the presence of the parallel flexure mechanisms and preload, the output displacement of the moving platform is smaller

than the nominal displacement of the PZT. The steady-state displacement of the moving platform in the Y direction can be represented by:

$$y = \frac{k_c k_{pzt}}{K_y k_c + k_c k_{pzt} + k_{pzt} K_y} s \quad (1)$$

where y is the output of the moving platform in the Y direction, and s is the nominal displacement of the PZT. When the preload is determined, the displacement of the stage is directly dependent on the output characteristics of the PZT. This indicates that the output accuracy of PZT will determine the positioning accuracy of the scanner.

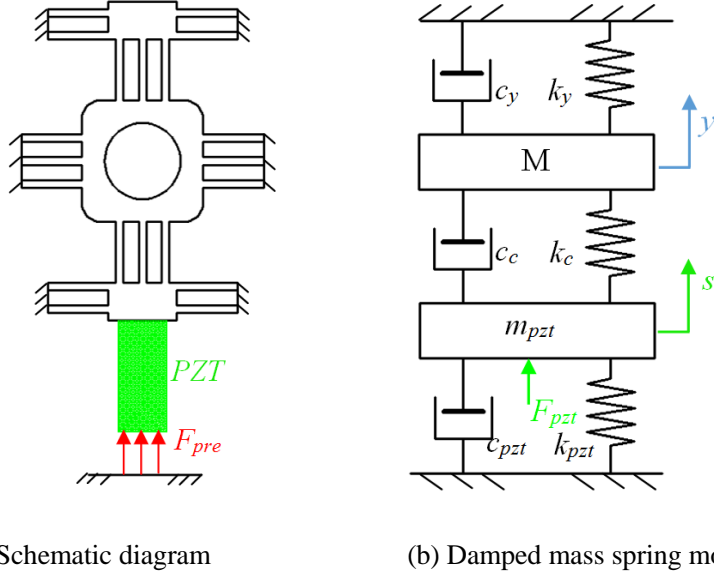


Figure 3. Schematic diagram and dynamic model of the piezo-driven flexure-based mechanism

Based on the Newton's second law of motion, the differential equation for dynamic motion of the XYZ scanner is given as follows:

$$\begin{bmatrix} M & 0 \\ 0 & m_{pzt} \end{bmatrix} \begin{bmatrix} \ddot{y} \\ \ddot{s} \end{bmatrix} + \begin{bmatrix} c_y + c_c & -c_c \\ -c_c & c_{pzt} + c_c \end{bmatrix} \begin{bmatrix} \dot{y} \\ \dot{s} \end{bmatrix} + \begin{bmatrix} K_y + k_c & -k_c \\ -k_c & k_{pzt} + k_c \end{bmatrix} \begin{bmatrix} y \\ s \end{bmatrix} = \begin{bmatrix} 0 \\ F_{pzt} \end{bmatrix} \quad (2)$$

As mentioned previously, the flexure hinge is an important component and has a close relationship with the natural frequencies of the scanner. From Equation (2), it is noted that the stiffness K_y is one of the key factors to determine the resonance frequency and the output displacement in the actuation direction. Thus, the stiffness of the hinge is the primary consideration for the mechanical design of the scanner.

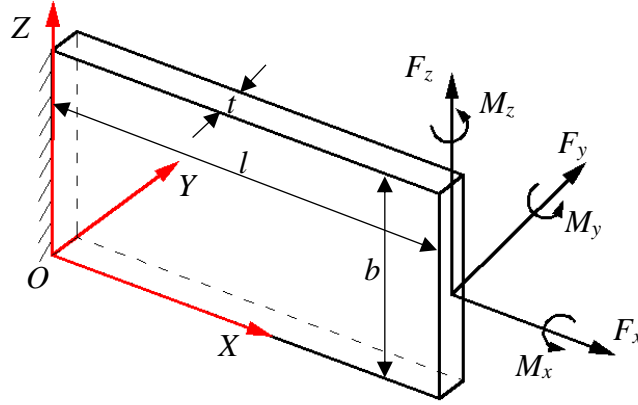


Figure 4. A single leaf flexure hinge

The stiffness of individual flexure was derived using strain energy method [30] and Castigliano's second theorem [31]. As shown in Fig. 4, the compliance matrix of a leaf flexure hinge can be defined as:

$$\begin{bmatrix} x \\ y \\ \theta_z \\ z \\ \theta_y \\ \theta_x \end{bmatrix} = \begin{bmatrix} C_{11} & 0 & 0 & 0 & 0 & 0 \\ 0 & C_{22} & C_{23} & 0 & 0 & 0 \\ 0 & C_{23} & C_{33} & 0 & 0 & 0 \\ 0 & 0 & 0 & C_{44} & C_{45} & 0 \\ 0 & 0 & 0 & C_{45} & C_{55} & 0 \\ 0 & 0 & 0 & 0 & 0 & C_{66} \end{bmatrix} \begin{bmatrix} F_x \\ F_y \\ M_z \\ F_z \\ M_y \\ M_x \end{bmatrix} \quad (3)$$

where $C_{11} = l/AE$, $C_{22} = l^3/3EI + \alpha l/GA$, $C_{23} = l^2/2EI$, $C_{33} = l/EI$, $C_{44} = 4l^3/Eb^3t + \alpha l/GA$, $C_{45} = 6l^2/Eb^3t$, $C_{55} = 12l/Eb^3t$, and $C_{66} = l/GJ$, t , b , and l are the thickness, width and length of the leaf flexure hinge, respectively, A , I and J are the cross-sectional area, the moment of inertia and polar moment of inertia of the hinge, respectively, E and G are the Young's modulus and the Shear modulus, respectively. α is a shape factor for the cross-section (for rectangular cross-section $\alpha = 6/5$).

Accordingly, the flexure displacement in the Y direction due to the applied force F_y and the moment $M_z = -F_y l/2$ can be calculated:

$$y = C_{22}F_y + C_{23}M_z = C_{22}F_y - C_{23}F_y l/2 \quad (4)$$

$$y = \left[\frac{l^3}{3EI} + \frac{\alpha l}{Gbt} - \frac{l}{2} \cdot \frac{l^2}{2EI} \right] F_y \quad (5)$$

Thus, the actuation stiffness is

$$k_y = \left[\frac{l^3}{12EI} + \frac{\alpha l}{Gbt} \right]^{-1} \quad (6)$$

Similarly, the displacement of the leaf flexure in the vertical Z direction is

$$z = C_{44}F_z + C_{45}M_y = C_{44}F_z - C_{45}F_z l/2 \quad (7)$$

$$z = \left[\frac{4l^3}{Eb^3t} + \frac{\alpha l}{Gbt} - \frac{l}{2} \cdot \frac{6l^2}{Eb^3t} \right] F_z \quad (8)$$

Thus, k_z can be obtained as

$$k_z = \left[\frac{2l^3}{Eb^3t} + \frac{\alpha l}{Gbt} \right]^{-1} \quad (9)$$

Therefore, the total actuation stiffness K_y and out-of-plane stiffness K_{out} of the XY stage can be calculated:

$$\begin{cases} K_y = k_y \cdot N \\ K_{out} = k_z \cdot N \end{cases} \quad (10)$$

Similarly, the total actuation stiffness K_z of the Z stage can be derived as

$$K_z = \left[\frac{5l^3}{6EI} + \frac{\alpha l}{Gbt} \right]^{-1} \cdot N \quad (11)$$

Therefore, during the design, l and b are first parameters determined according to the requirement of the mechanical design. Since the hinges must be located inside the small and compact scanner, all dimensional parameters should consider the size and arrangement issues. Furthermore, it should also consider the specification of the required working range of the scanner. A key design specification for a high-speed scanner is a higher resonance frequency, and thus broad bandwidth is achieved by increasing the stiffness of the flexure mechanism. However, this will inevitably result in the reduction in the motion range. Therefore, it is necessary to have tradeoff between the resonance frequency and motion range of the scanner. Based on the design requirements, manufacturing capability and repeatability, the dimensional parameters can be determined as follows: $t = 1$ mm, $l = 8$ mm, $b = 20$ mm (the XY stage), and $t = 1$ mm, $l = 3.5$ mm, $b = 2.9$ mm (the Z stage). Substituting these values

into Equations (10), and (11), the stiffness K_y , K_{out} and K_z can be calculated and plotted as shown in Fig. 5.

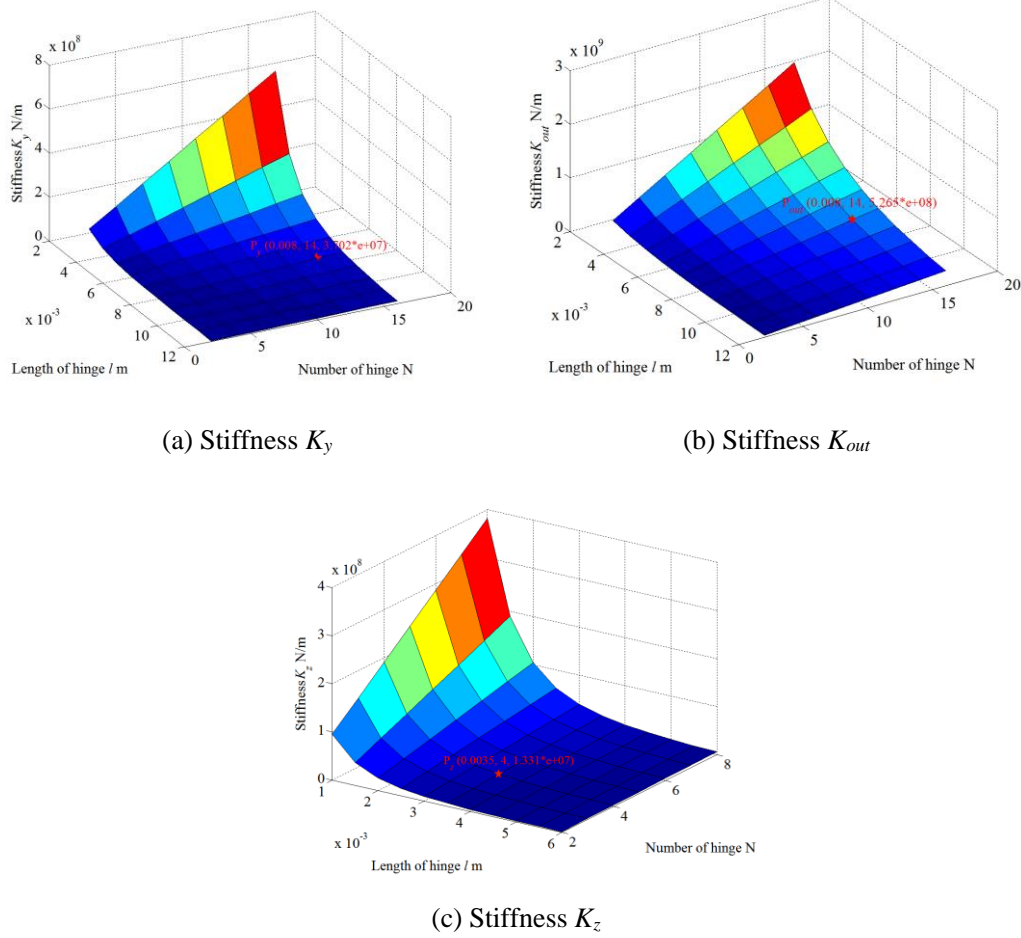


Figure 5. Relationship between stiffness K_y , K_{out} , and K_z and the flexure hinge parameters

3. Model verification and prototype development

3.1 Model Verification

In order to validate the established models and obtain further insights into the static and dynamic characteristics of the developed scanner, finite element analysis (FEA) was conducted using ANSYS software package. The scanner is fabricated using Aluminum 7075-T6 with a density of $2,770 \text{ kg/m}^3$, a Young's modulus of 71 GPa , a Poisson's ratio of 0.34 and a yield strength of 434 MPa . In order to improve the computational accuracy, mapping mesh method is utilized and strictly controlled and refined in the areas of flexure hinges and PZTs, where the large deformation generally occurs (shown in Fig. 6).

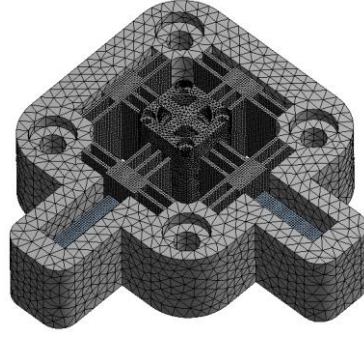


Figure 6. Finite element model of the scanner.

In order to investigate static characteristics of the scanner, the FEA was conducted by applying a displacement at the moving platform in the three working directions. With an applied $8\mu\text{m}$ displacement, the computational deformation and stress results in the X direction are illustrated in Fig. 7. It can be seen that the generated stress is much smaller than the material allowable stress. Thus, the maximum reachable workspace is determined by the material allowable stress and can be obtained as $135 \times 135 \times 154 \mu\text{m}^3$ through the FEA. It is noted that the linear stiffness without PZTs installed are $27.39 \text{ N}/\mu\text{m}$, $27.65 \text{ N}/\mu\text{m}$, and $10.41 \text{ N}/\mu\text{m}$ in the X, Y and Z directions, respectively. However, the out-of-plane stiffness of the XY stage is a key factor for determining its capacity of resisting disturbance in the vertical direction. The computational analyses show that an out-of-plane stiffness of $181.2 \text{ N}/\mu\text{m}$ can be achieved. Thus, the out-of-plane stiffness of the central moving platform of the XY stage is larger than that of the Z stage. Further, comparison of the results of theoretical and computational analyses, it is noted that the analytical models generate relatively large deviations in stiffness prediction due to the model simplification and over-constraining of the flexure mechanism.

To further examine the dynamic performance of the developed scanner, modal analysis has been conducted using FEA. During the simulations, PZT was considered as the actuation element with a constant stiffness. One end of the actuator was fixed and the other end was attached to the input point of the flexure mechanism. The modal analysis results reveal that the first three natural frequencies of the scanner are $6,886.04 \text{ Hz}$, $6,887.13 \text{ Hz}$, and $29,464 \text{ Hz}$, respectively. As shown in Fig. 8, the mode

shapes of the first two natural frequencies are the translations along the X and Y directions, and the third one is the translation of the moving platform along the Z direction. The similar values of the first two natural frequencies imply that the XY stage has almost identical dynamic characteristics in the X and Y directions. The computational results confirm that the scanner has three translational degrees of freedom and the first lateral resonance frequency of 6.8 kHz is approximately eight times higher than that of traditional piezoelectric tube, and thus it can provide a broad bandwidth for the application of high speed scanning.

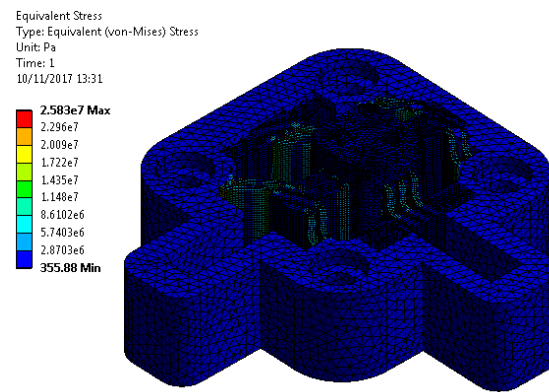


Figure 7. Finite element result of the scanner

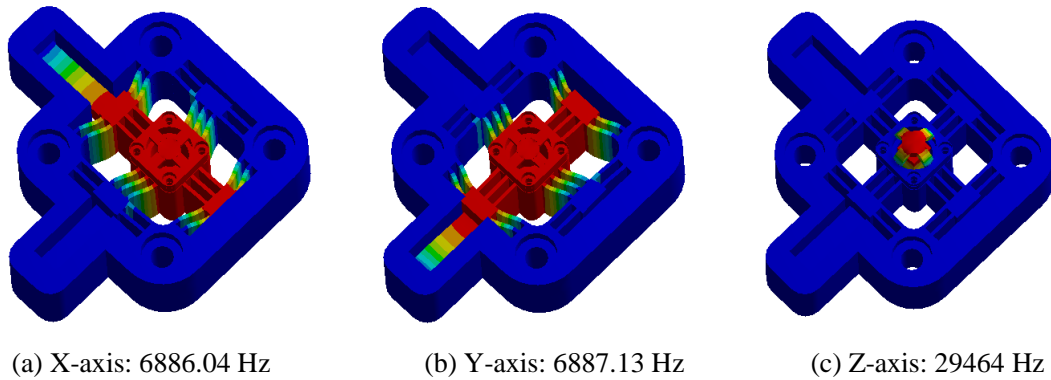


Figure 8. Modal analysis of the scanner with PZTs

3.2 Prototype development and experimental studies

The developed prototype of the scanner is shown in Fig. 9. The top and bottom surfaces were fabricated by face milling to guarantee the parallelism. Artificial aging treatment was utilized to release the residual stress. Computer numerical control (CNC) assisted wire electrical discharge machining (WEDM) technique was utilized

to manufacture all the flexure structures. During the WEDM fabrication process, low feed rate was selected to guarantee the machining accuracy, and a fabrication tolerance of $2\text{ }\mu\text{m}$ was achieved. The XY stage and Z stage were separately fabricated and assembled together using bolted connections to form the XYZ scanner. Based on Equation (1), it is noted that the output displacement of the moving platform will be less than the nominal displacement of the PZT due to the stiffness of the flexure hinges. The FEA results also suggest that the PZT should be chosen as to ensure an effective motion range, and thus meet the requirements of the scanning tasks. The PZT (model: PZS001 $6\text{ mm} \times 7\text{ mm} \times 20\text{ mm}$, from THORlabs, Inc.) was selected to provide a nominal displacement of $17.4\text{ }\mu\text{m}$ and resonance frequency of 69 kHz . The piezoelectric amplifier was chosen as the THORlabs (MDT693A) with the gain of $7.5\sim 15$.

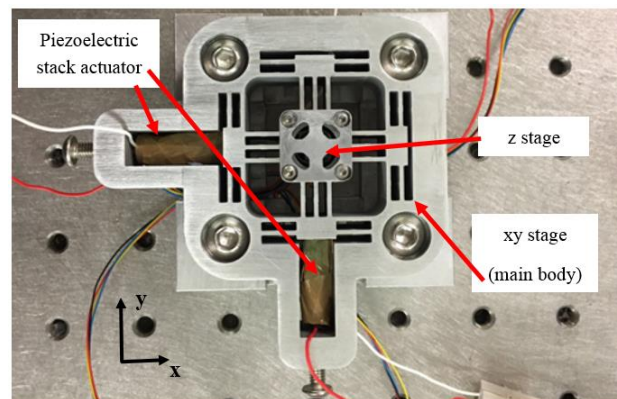


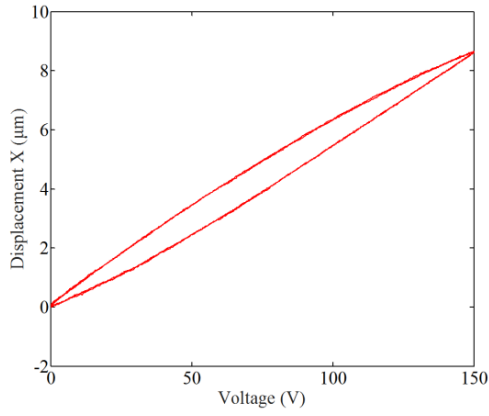
Figure 9. Manufactured prototype of the XYZ scanner.

The output motion of the scanner in each axis was measured by PI (D510.021) single-electrode capacitive sensor with a measurement range of $20\text{ }\mu\text{m}$ and a resolution of 0.2 nm . The PI (E-509.E03) amplifier was utilized to modulate and filter the raw measurement data. The command signal of the motion and the data acquisition tasks were implemented using a NI acquisition card USB-6251 via the Labview interface. The entire experimental investigation was conducted on a Newport RS-4000 vibration isolation table in order to reduce the external disturbances.

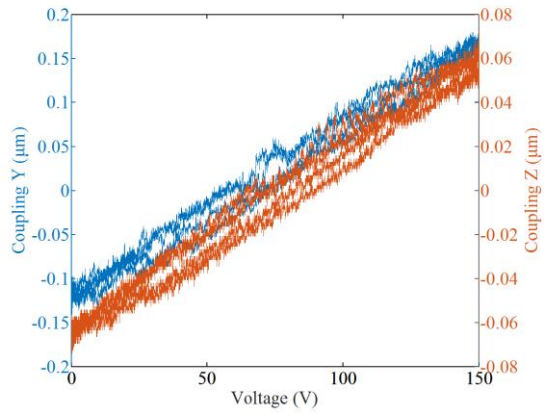
The effective motion range and cross-coupling effects of the scanner in the three directions were examined through a number of experiments. By applying a sinusoidal command signal (frequency 1 Hz and 150 V p-p) to the PZT in the X (Y or Z) axis,

the moving platform of the scanner will be actuated to translate along the X (Y or Z) direction. Then, the displacement in the three axes were simultaneously measured to determine the motion range and crosstalk among the three directions. The experimental testing under open loop control has been conducted and the measured results are shown in Fig. 10. It is worth noting that the proposed scanner has approximately the effective workspace of $8.66 \times 8.4 \times 10.6 \mu\text{m}^3$. The actual output displacement of the scanner is smaller than the nominal displacement of PZT ($17.4 \mu\text{m}$). This is due to the presence of the flexure hinge mechanisms and preload for PZTs. The actual steady-state displacement of the scanner is in agreement with the result of theoretical Equation (1). In addition, it can be seen that the maximum coupling effect is 1.8 % between the three working axes. These are mainly due to the manufacture and assembly errors, and the preload induced asymmetry of the flexure structure. It is noted that from Fig. 11(a), (c) and (e), there obviously exists hysteresis in the output displacement of the three axes. Both the cross-coupling effects and hysteresis errors will generally affect the positioning accuracy of the scanner. In order to reduce/eliminate the nonlinearity and cross-coupling errors, and thus improve the performance of the proposed scanner, a closed-loop feedback and compensation control scheme will be developed and presented in the Section 4.1.

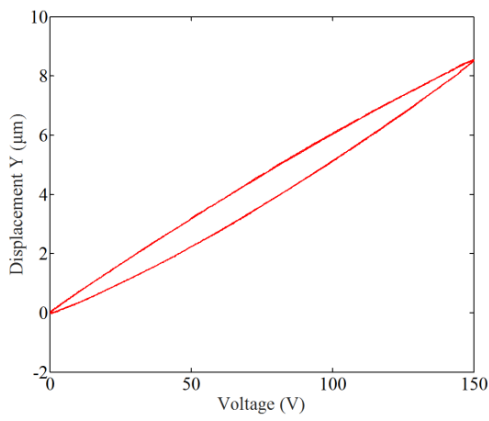
The resolution of the developed scanner has been examined and shown in Fig. 11. The resolution is determined by the noise level of the entire electromechanical system and the performance of the D/A converter. By strictly controlling the noise level and increasing the resolution of D/A converter, the resolution of the scanner can be further improved. In the current design, 16 bit D/A converter was utilized in the control system. The corresponding resolutions of the developed scanner are 7 nm, 7 nm, and 5 nm in the X, Y and Z directions, respectively. If the noise level can be further reduced, thus higher resolution can be obtained.



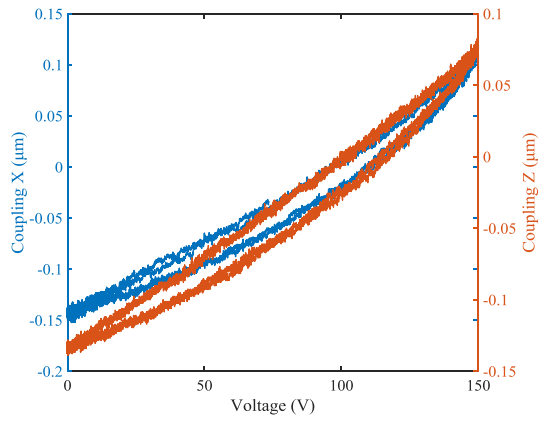
(a) Motion range of X-axis



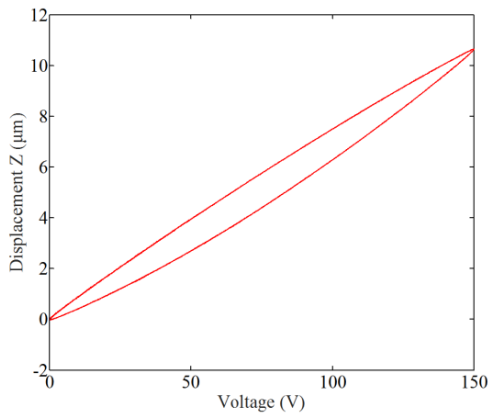
(b) Corresponding coupling errors of Y and Z axes



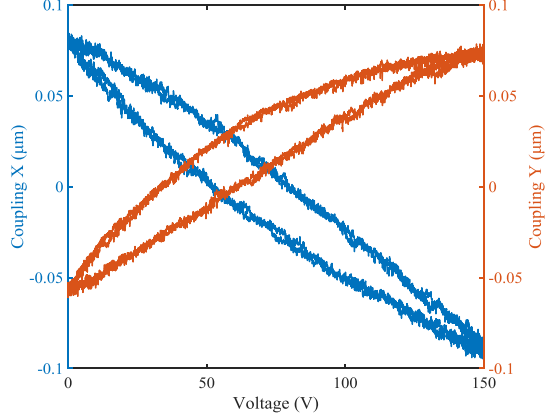
(c) Motion range of Y-axis



(d) Corresponding coupling errors of X and Z axes

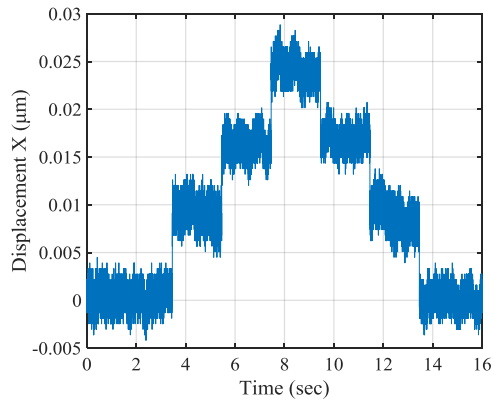


(e) Motion range of Z-axis

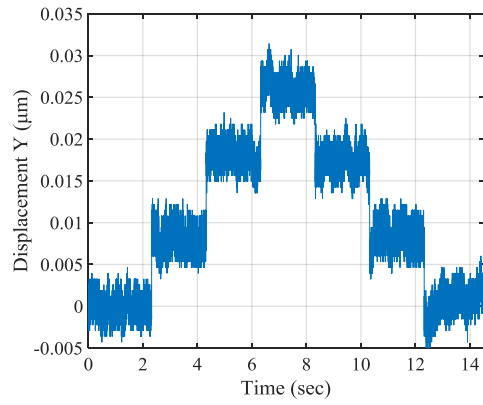


(f) Corresponding coupling errors of X and Y axes

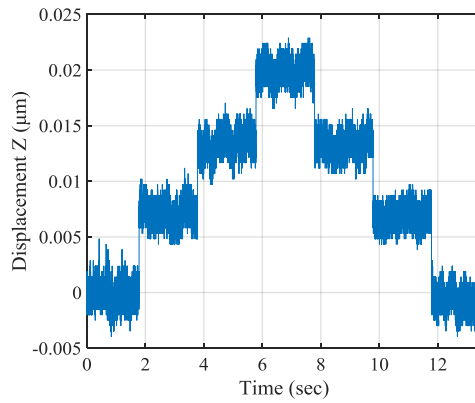
Figure 10. Results of the motion range and cross-coupling effects



(a) Resolution in the X-axis



(b) Resolution in the Y-axis



(c) Resolution in the Z-axis

Figure 11. Resolution in the X, Y, and Z axes of the developed scanner

4. Controller design and implementation

The controller schematic diagram and experimental setup are illustrated in Fig. 12. To measure the displacement of the PZT, four strain gauges were attached on each of the actuator to form a full Wheatstone bridge. The strain of the actuator was measured and processed with a Dynamic Strain Gauge amplifier (SDY2105). To build a compact high-speed scanner, the PI (D510.021) single-electrode capacitive sensors were only used for measurement and calibration of the scanner, and were replaced with the full bridge strain gauges when the scanner was installed in the home-made AFM. This indicates that a semi-closed loop feedback will be utilized in the high speed AFM. The implementation of the control algorithm was carried out by an Anadigm® FPAA QUADAPEX development board (four AN231K04) which is based on integrated switched capacitor technology. The FPAA based controller was

implemented directly for analog signals, unlike digital controller where the signals need to be sampled and quantized using A/D converter before sending to DSP processor. This conversion and quantization will inevitably affect the speed and accuracy of the control system. Thus, the FPAA based technique is equivalent to a direct analog implementation of the controller and allows for a broad bandwidth operation. The analog arrays are made of switched capacitors with switching frequencies up to 16 MHz, which reduces/eliminates the effects of sampling and quantization.

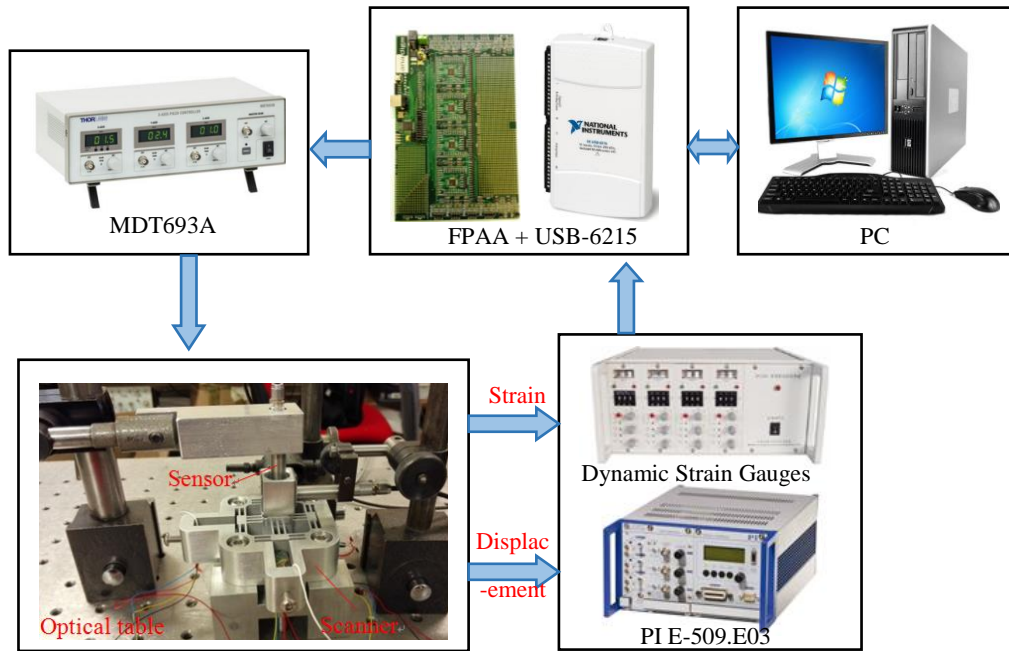


Figure 12. Experimental setup of the XYZ scanner.

4.1 Controller design

Due to the hysteresis and creep of PZT, the relationship between the applied voltage and the output displacement of PZT is nonlinear, as shown in Fig.10. In order to reduce the hysteresis effect, many models have been developed to describe the nonlinearities [32-36]. The Bouc-Wen model is one of such kinds of hysteresis models to describe the hysteresis loop [37, 38]. The governing equation of the Bouc-Wen model is given as:

$$\dot{h} = a d_e \dot{V}_{pzt} - b \left| \dot{V}_{pzt} \right| h - c \dot{V}_{pzt} |h| \quad (12)$$

where a , b and c are the parameters to determine the shape of the hysteresis loop, h is the hysteresis variable. These parameters can be identified based on the experimental study and the nonlinear least square fit method.

The block diagram of the control system with hysteresis compensation is shown in Fig. 13(a). The inverse Bouc-Wen model can be cascaded to the physical system as a feedforward controller for the hysteresis compensation. In order to improve the robustness and stability of the developed scanner, a feedback controller is essential to reduce the effects of external disturbances and the unmodeled errors. Therefore, a proportional-integral (PI) controller was employed to form a hybrid feedforward-feedback controller for the developed scanner. The schematic diagram of the hybrid controller is illustrated in Fig. 13(b). The implementation of the proposed hybrid control algorithm was implemented through FPAA development kit with 16 MHz oscillation module. Fig. 14 shows the circuit diagram developed using AnadigmDesigner[®] software, which will be downloaded to the FPAA board for the hybrid feedforward/feedback control for the scanner.

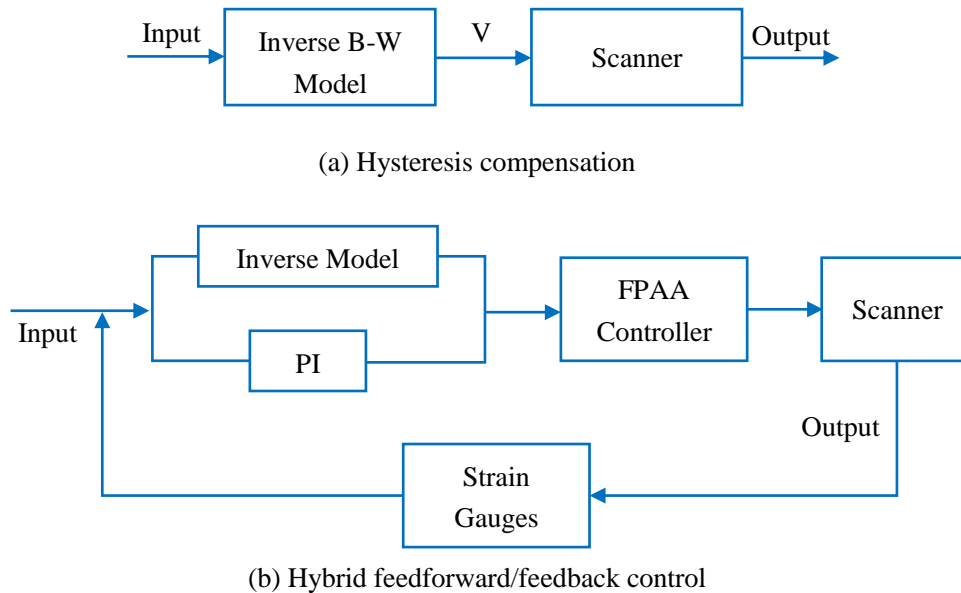


Figure 13. Block diagram of control system for the developed scanner

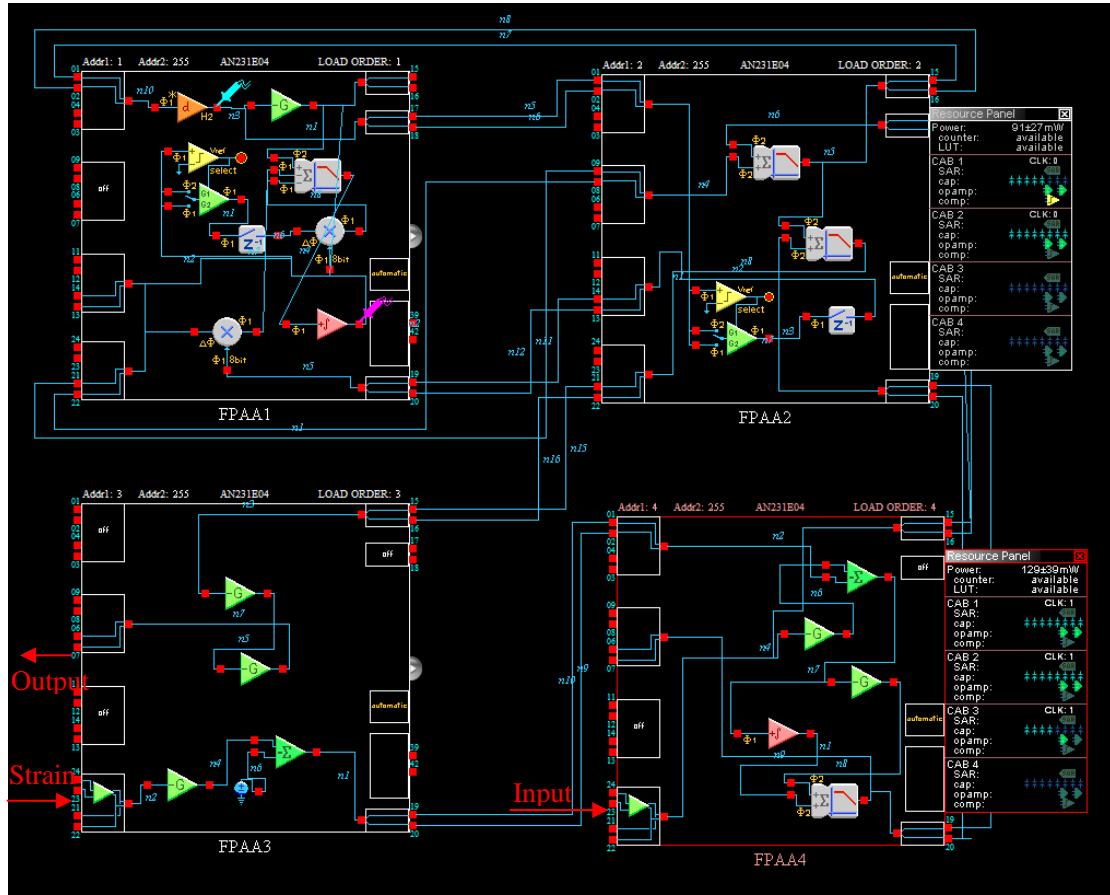


Figure 14. Implementation of the hybrid control on the FPAA

Based on the hybrid controller, the trajectory tracking of the developed controller was examined to validate the performance of the control strategy. As shown in Fig. 15, a sinusoidal trajectory with the amplitude of $4 \mu\text{m}$ and frequency of 10 Hz was utilized to investigate the tracking performance in the X direction. Compared with Fig. 10(a), it is noted that the feedforward controller can effectively reduce the hysteresis and improve the linearity, as shown in Fig. 15(a). The tracking performance can be further improved using the hybrid feedforward/feedback controller as shown in Fig. 15(b). In order to examine the tracking capability for complex trajectory, a command signal generated from multi-frequency sinusoidal superposition was utilized to drive the developed scanner. The tracking performance was evaluated and shown in Fig. 16. The time history shows that the scanner can exactly follow the command signal and the maximum tracking error is approximately 70 nm. The relationship between the input and the output is approximately linear, and thus hysteresis has been significantly reduced and/or eliminated. These experimental results validate that the developed

hybrid controller has excellent characteristics for the applications in piezo-driven scanner.

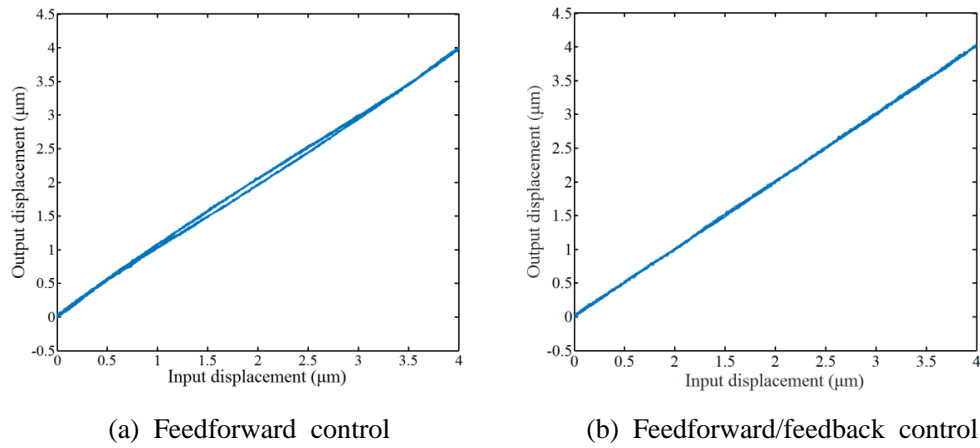


Figure 15. Results of sinusoidal trajectory tracking in the X axis of the controller

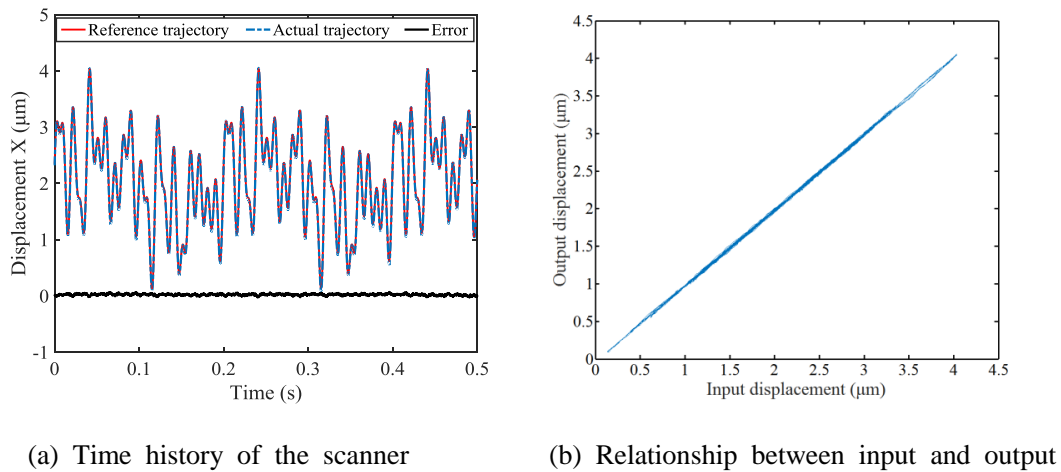
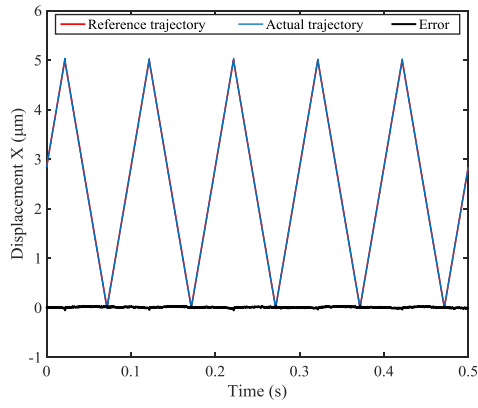


Figure 16. Complex trajectory tracking in the X axis of the controller

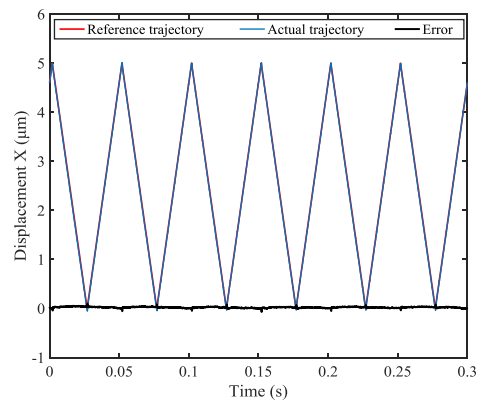
4.2 Trajectory tracking of the XYZ scanner

To examine the tracking ability of the XYZ scanner under the hybrid control method, a number of trajectory tracking experiments were conducted. Fig. 17 shows the experimental results for the triangle wave trajectories. For the X and Y axes, three triangle wave trajectories with the same amplitude of 5 μm and frequencies of 10 Hz, 20 Hz and 50 Hz were utilized. As shown in Fig. 17 (a-f), the maximum tracking errors under the command signal of the frequency of 50 Hz are less than $\pm 0.15 \mu\text{m}$, indicating the relative error is less than 3%. Fig. 18 (a-c) shows the tracking results of the Z axis for the three triangle wave trajectories. It is noted that the maximum

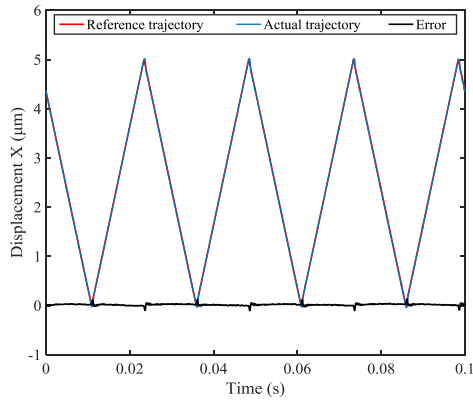
tracking errors are $\pm 0.038 \mu\text{m}$, $\pm 0.056 \mu\text{m}$ and $\pm 0.12 \mu\text{m}$ under the frequency of 10 Hz, 20 Hz and 50 Hz. This indicates that relative displacement errors are as small as 0.76%, 1.12 % and 2.4 %. With consideration of the requirements for Z axis, the measured surface profile need to be tracked, and thus the complex trajectory tracking capability should be examined. Fig. 18(d) shows the tracking characteristics of the Z axis for the signal of multi-frequency sinusoidal superposition. It is noted that the maximum tracking errors is $\pm 0.04 \mu\text{m}$, which indicates that the scanner has the capability to track complex signals with high accuracy.



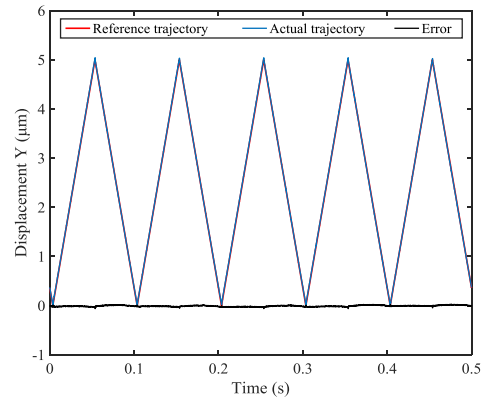
(a) X-axis: 10 Hz



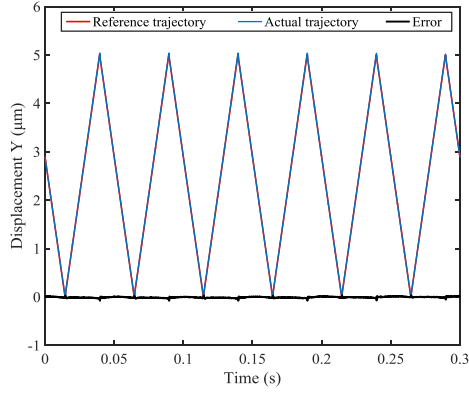
(b) X-axis: 20 Hz



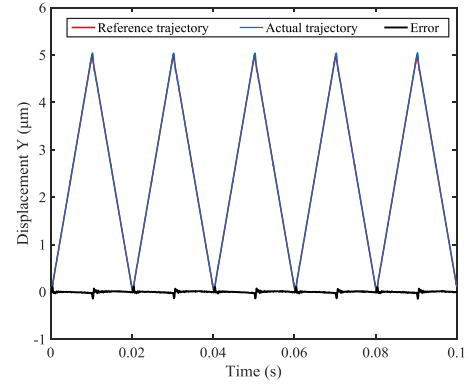
(c) X-axis: 50 Hz



(d) Y-axis: 10 Hz

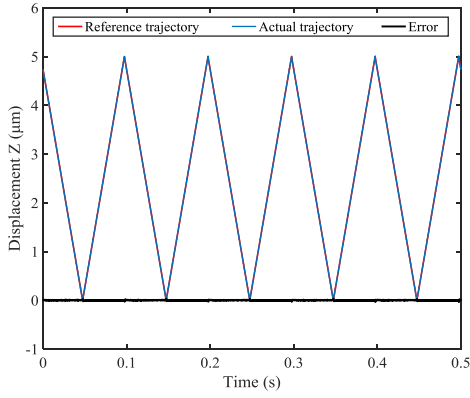


(e) Y-axis: 20 Hz

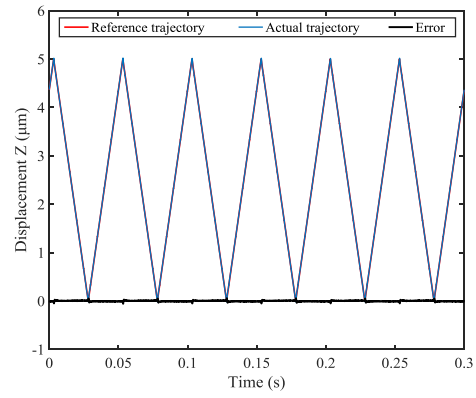


(f) Y-axis: 50 Hz

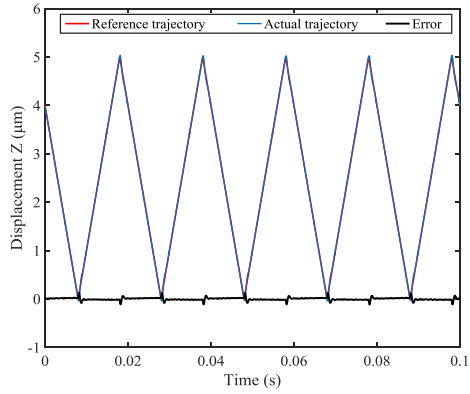
Figure 17. Tracking results in the X and Y axes of the developed scanner



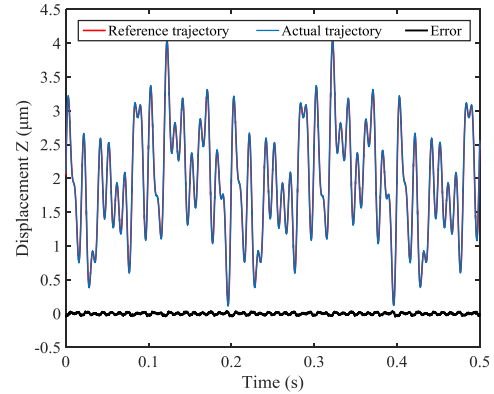
(a) 10 Hz



(b) 20 Hz



(c) 50 Hz



(d) Complex trajectory

Figure 18. Tracking results in the Z axis of the developed scanner.

In order to investigate the scanning capability of the scanner within the entire workspace, a series of triangle wave trajectories with different amplitudes and same frequencies of 50 Hz were applied to the X, Y and Z axes. The tracking errors are

obtained and shown in Table I. It is noted that the maximum relative errors of the X, Y and Z axes are respectively 5.1%, 5.6% and 4.3% for 0.4 μm amplitude command signal. The relative errors reduce with the increasing of the amplitude of the command signals. This indicates that the nonlinearity of the PZT has been significantly reduced with the aid of the hybrid feedforward/feedback controller.

Table I. Tracking errors of the scanner

Displacement (μm)	Maximum Error		
	X-axis	Y-axis	Z-axis
0.4	5.1%	5.6%	4.3%
0.8	4.3%	4.5%	3.6%
1	3.2%	3.5%	2.1%
3	2.8%	3.1%	2.3%
7	3.1%	3.3%	2.8%

5. AFM imaging

Based on the developed scanner, a home-made AFM has been proposed for high speed imaging. The 3 dimensional model of the AFM is shown in Fig 19. A 3-axis motion stage (MTS25-Z8, from THORlabs, Inc.) was used to implement large range movement and coarse positioning. The developed scanner was utilized for the high speed scanning and topography measurement. A laser diode was used to generate laser beam and the quadrant photodiodes (QP, QP50-6-18u-SD2, First Sensor) utilized for the displacement detection. A National Instrument (NI) control board (USB-6215) was used to implement the sensing, measurement and motion control of the developed AFM. To measure the surface profile using contact mode, the deflection of the cantilever remains constant by controlling the output of the Z axis of the scanner based on the detected displacement of cantilever. The schematic diagram of control system is shown in Fig. 20. The overall geometric size of the AFM is $311 \times 239 \times 237 \text{ mm}^3$ and the total weight 4.2 kg. In order to reduce the external disturbance,

an active vibration isolation device (VAIS-BUDGET) is used to support the home-made AFM. The entire assembly is mounted on the optical vibration isolation table which will ensure the reduced noise level of the cantilever.

In order to investigate the performance of the proposed AFM, a standard calibration grating (MikroMasch TGZ2) with the period of $3\text{ }\mu\text{m}$ and the height of 108 nm was used to examine the imaging accuracy. The grating was mounted on the moving platform of the scanner and the raster scanning was utilized by supplying the scanner with pure triangular waveforms with the frequencies of 10 Hz, 30 Hz, 50 Hz, 70 Hz and 100 Hz. The ContAl cantilever from Budget Sensors was utilized to provide the first resonance frequency of 13 KHz and stiffness of 0.2 N/m. The topographic image of the grating was constructed from the driving signal to the Z axis of the scanner under the PID control strategy. The X axis of the scanner is chosen as the fast scanning direction, and the Y axis the slow scanning direction. The hybrid feedforward/feedback control strategy is used in the fast scanning direction, and the open loop control in the slow scanning direction.

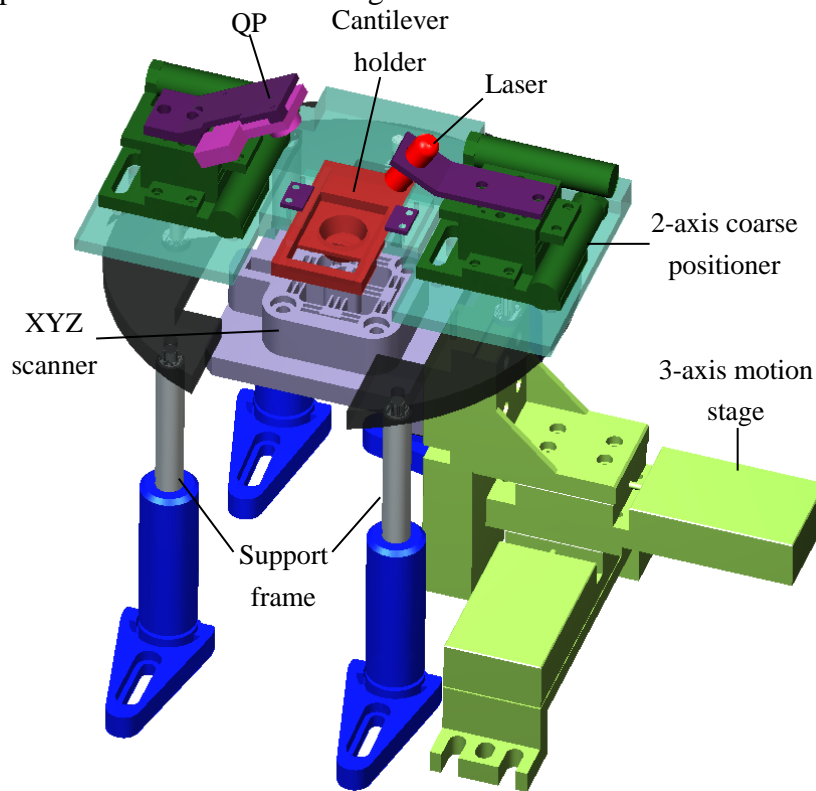


Figure 19. 3D model of the home-made AFM

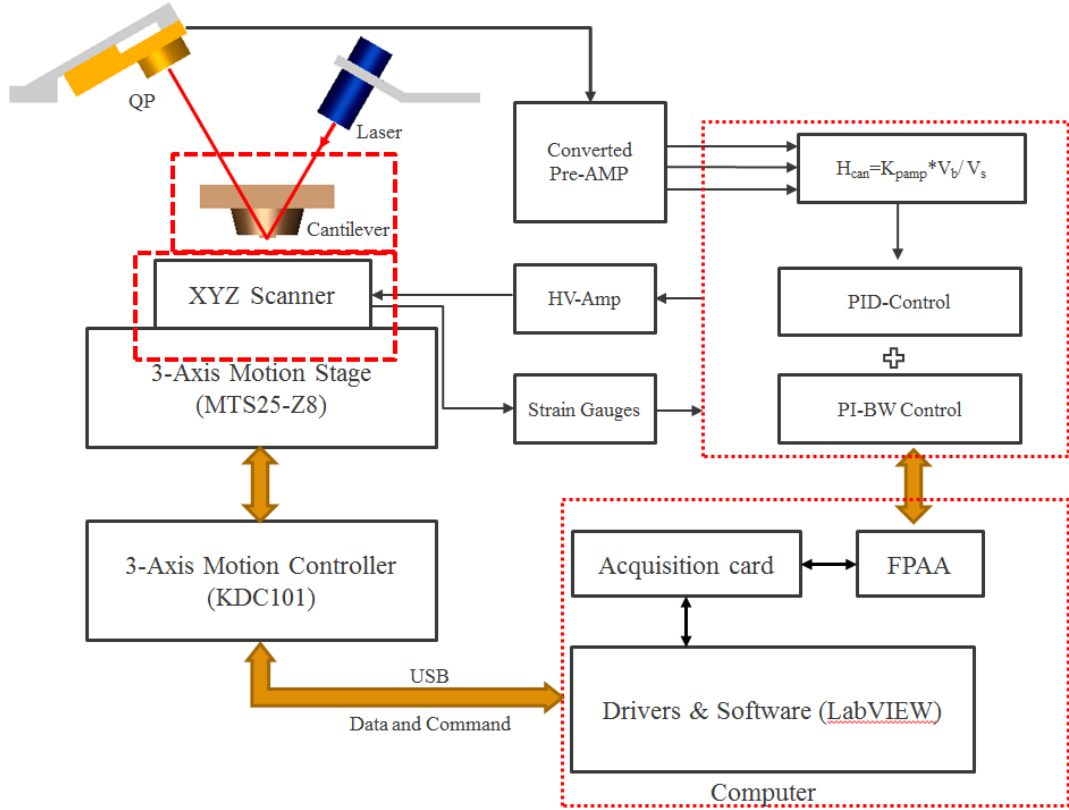
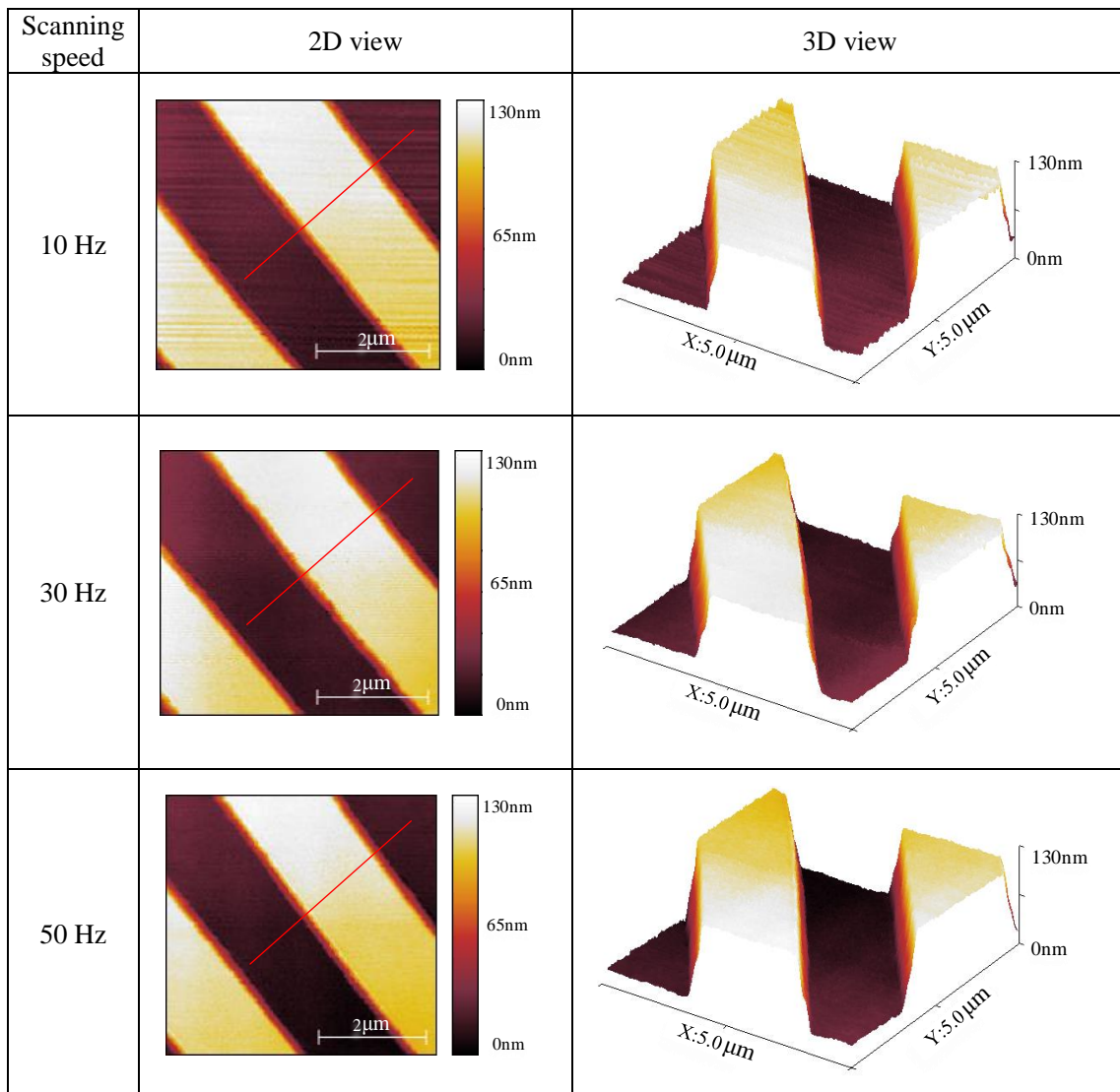


Figure 20. Schematic diagram of the detection and control system for the AFM

Figure 21 shows the images obtained with the proposed AFM. An area of $5 \times 5 \mu\text{m}^2$ of the grating was measured for a pixel resolution of 512×512 with line rates of 10 Hz, 30 Hz, 50 Hz, 70 Hz and 100 Hz. It is noted that the developed AFM can image the grating with different scanning speeds. However, there are some artifacts and noises in the images. The influences of these errors will increase with the increasing scanning speed. In order to improve the signal fidelity, slow scanning should be utilized to make the tip track the surface accurately. However, high speed scanning is important for the live cell imaging. Therefore, it is necessary to trade off the scanning speed and the imaging quality. Since the raw data have been used for these images, the noise can be removed through signal filtering. The artifacts at the edges of the grating are the inherent characteristics for high aspect ratio surface measurement. This is due to the tip bridge and tip flight effects on the imaging of the surface topography. It can also be seen that the oscillations in the slow scanning direction is obvious due to the open loop control in the Y axis.

The profiles along the red lines in Fig. 21 are utilized to illustrate the difference between the measured results under different scanning speeds, as shown in Fig. 22. It is noted that the height of 104 nm and the period of 3.2 μm have been identified through all these measurements. The measurement errors may be due to the calibration of the scanner and the manufacturing errors of the grating. However, the edge artifacts, bridging effects and noises increase with the increasing scanning speed. These are in agreement with the intuitional knowledge for the AFM tip-based imaging.



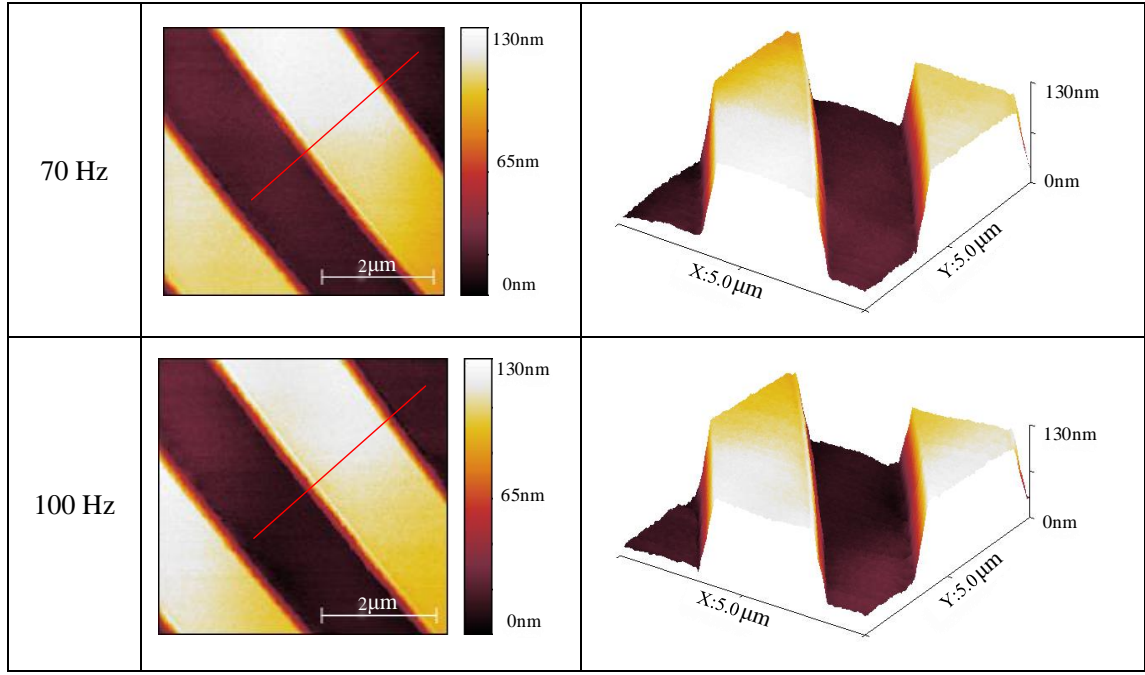


Figure 21. 3D images of the grating scanning

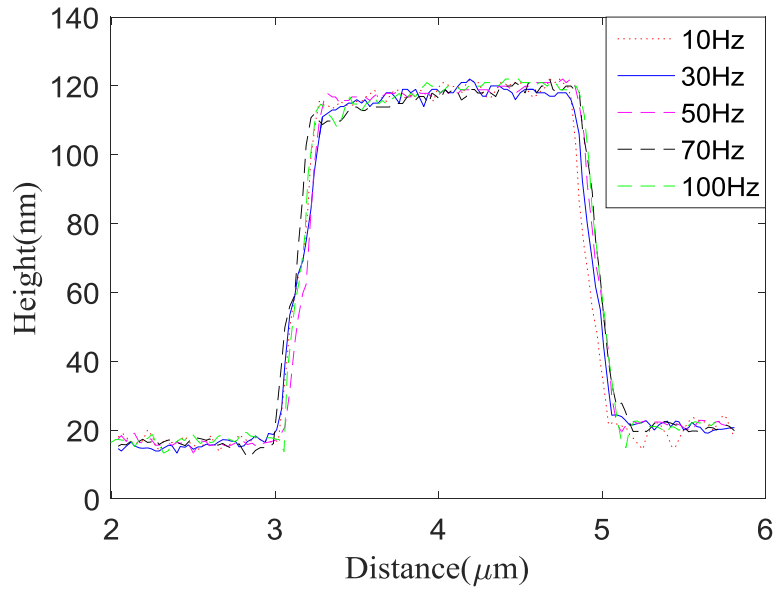
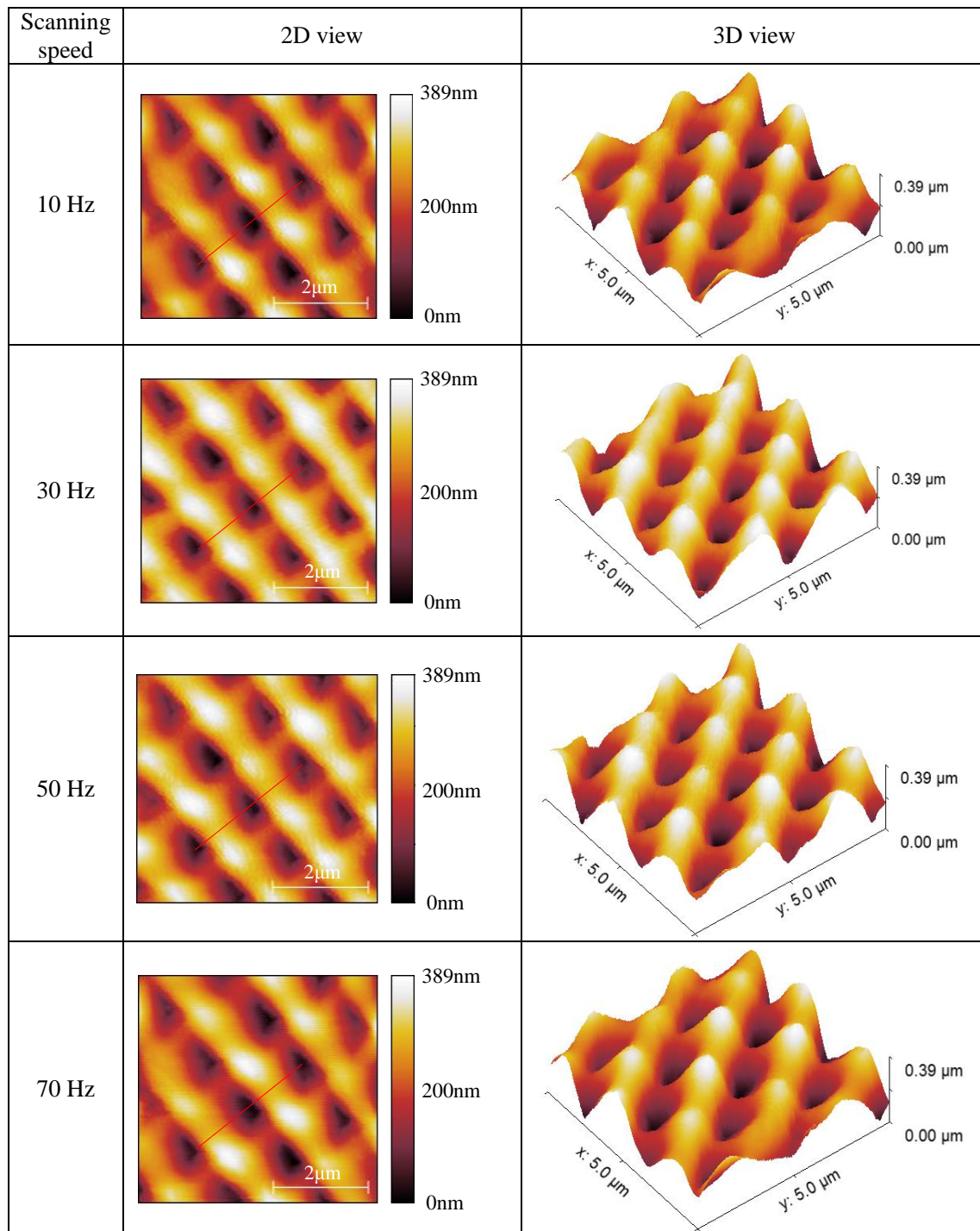


Figure 22. Profiles at different scanning speeds

A two dimensional sinusoidal grating (Benyan, China) with the period of $1.67 \mu\text{m}$ and amplitude 330 nm was also utilized to examine the imaging performance of the developed AFM. The measured images with different scanning speeds are shown in Fig. 23. Compared with the images of Fig. 22, the imaging quality has been improved for the sinusoidal grating measurement using the same scanning parameters. This is mainly due to the reduction of tip flight phenomena, induced by the high

aspect ratio surface. However, it is noted that the bridge effects and tip flight will affect the shape of the measured surface (shown in Fig. 24). The obtained profile has the flat peaks and sharp valleys compared with the normal sinusoidal profile. The noise level will also increase with the increasing scanning speed.



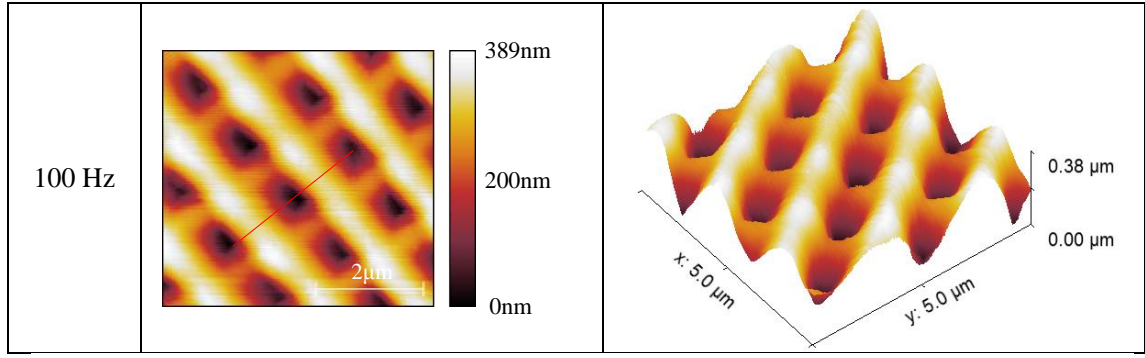


Figure 23. 3D images of sinusoidal grating measurement

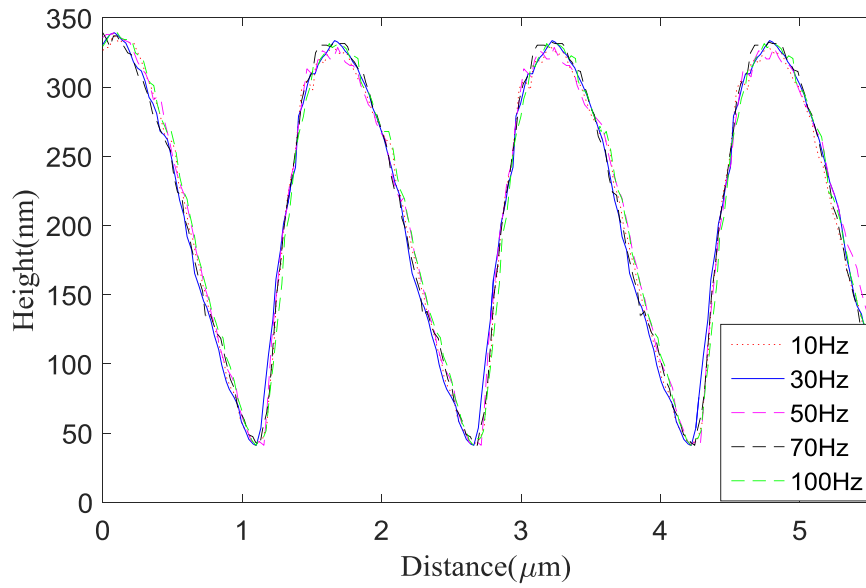


Figure 24. Measured profiles of sinusoidal grating at different scanning speed

In order to examine the full range of scanning capabilities of the developed AFM, two small areas ($3 \times 3 \mu\text{m}^2$ and $2 \times 2 \mu\text{m}^2$) have been scanned under the scanning frequency of 50 Hz, as shown in Fig. 25. The line grating image is shown in Fig. 25(a). It is noted that the edge artifacts exists due to the tip flight and tip bridging effects at these sections. For the sinusoidal grating imaging (shown in Fig. 25(b)), the tip flight effects are significantly reduced, however, the tip bridging effects can be clearly over-represented due to the deep valleys of the sample. There still exist some noises and errors in these images, and these may be due to the external disturbance and the inherent dynamics of the AFM induced by the high aspect ratio surfaces.

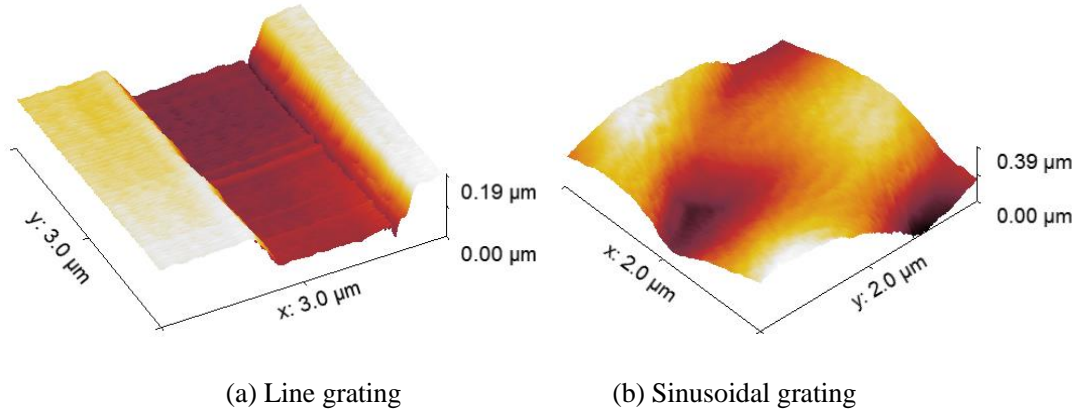


Figure 25. 3D height images of small area scanning

6. Conclusion

The mechanical design of a broad bandwidth flexure-based XYZ scanner has been investigated. Detailed parametric design has been performed, and FEA has been utilized to validate the static and dynamic characteristics of the proposed scanner. The scanner has the resonance frequencies at 6.8 kHz in the X- and Y-axes, and 29 kHz in the Z-axis. A number of experimental studies were conducted to examine the characteristics of the scanner. It was illustrated that an effective workspace of $8.66 \times 8.4 \times 10.6 \mu\text{m}^3$ can be achieved and the cross-coupling errors are less than 1.8%. The tracking performance of the scanner was improved using the hybrid feedforward/feedback control strategy. Combined with the proposed scanner and FPAA control technique, a simple, compact, and highly integrated AFM has been constructed. High speed scanning has been implemented to investigate the performance of the developed scanner for standard grating measurement with the scanning frequency of up to 100 Hz and resolution of 512×512 pixels. Due to the broad bandwidth of the scanner and the advantages of the FPAA controller which allows analog implementation of the control algorithm, high speed AFM scanning can be achieved by the developed scanner. Future research efforts will be directed towards implementing biaxial closed-loop control to reduce external disturbances, and broad bandwidth Z axis tracking strategy and trajectory planning for high speed scanning, and thus further improving the imaging quality.

Acknowledgement

This work is supported by the National Natural Science Foundation of China (No. 51675367, 51675371), EU H2020 MSCA RISE 2016 (No.734174).

References

- [1] T. Ando. "High-speed AFM imaging." *Current opinion in structural biology* 28 (2014): 63-68.
- [2] B. Vasić, A. Matković, R. Gajić, and I. Stanković. "Wear properties of graphene edges probed by atomic force microscopy based lateral manipulation." *Carbon* 107 (2016): 723-732.
- [3] S. S. Park, M. G. Mostofa, C. I. Park, M. Mehrpouya, and S. Kim. "Vibration assisted nano mechanical machining using AFM probe." *CIRP Annals-Manufacturing Technology* 63, no. 1 (2014): 537-540.
- [4] N. Yeow, R. F. Tabor, and G. Garnier. "Atomic force microscopy: From red blood cells to immunohaematology." *Advances in Colloid and Interface Science* (2017).
- [5] Y. F. Dufrêne, D. Martínez-Martín, I. Medalsy, David Alsteens, and Daniel J. Müller. "Multiparametric imaging of biological systems by force-distance curve-based AFM." *Nature methods* 10, no. 9 (2013): 847-854.
- [6] S. Kalinin and A. Gruverman. *Scanning probe microscopy: electrical and electromechanical phenomena at the nanoscale*. New York: Springer Science and Business Media, 2007.
- [7] M. Lanza. *Conductive Atomic Force Microscopy: Applications in Nanomaterials*. Wiley-VCH, 2017.
- [8] P. Eyben, M. Xu, N. Duhayon, T. Clarysse and S. Callewaert. "Scanning spreading resistance microscopy and spectroscopy for routine and quantitative two-dimensional carrier profiling." *Journal of Vacuum Science & Technology B: Microelectronics and Nanometer Structures Processing, Measurement, and Phenomena* January 20, no. 1 (2002): 471-478.
- [9] Y. K. Yong, and S. R. Moheimani. "Collocated Z-axis control of a high-speed nanopositioner for video-rate atomic force microscopy." *IEEE Transactions on Nanotechnology* 14, no. 2 (2015): 338-345.
- [10] T. Ando, Takayuki Uchihashi, Noriyuki Kodera, Daisuke Yamamoto, Masaaki Taniguchi, Atsushi Miyagi, and Hayato Yamashita. "High-speed atomic force microscopy for observing

- dynamic biomolecular processes.” *Journal of Molecular Recognition* 20, no. 6 (2007): 448-458.
- [11] T. Ando, Takayuki Uchihashi, Noriyuki Kodera, Daisuke Yamamoto, Atsushi Miyagi, Masaaki Taniguchi, and Hayato Yamashita. “High-speed AFM and nano-visualization of biomolecular processes.” *Pflügers Archiv-European Journal of Physiology* 456, no. 1 (2008): 211-225.
- [12] A. A. Tseng. “Advancements and challenges in development of atomic force microscopy for nanofabrication.” *Nano Today* 6, no. 5 (2011): 493-509.
- [13] J. A. Vicary, M. J. Miles. “Real-time nanofabrication with high-speed atomic force microscopy.” *Nanotechnology* 20, no. 9 (2009): 095302.
- [14] T. Ando, T. Uchihashi, and T. Fukuma. “High-speed atomic force microscopy for nano-visualization of dynamic biomolecular processes.” *Progress in Surface Science* 83, no. 7 (2008): 337-437.
- [15] Olympus, see <http://probe.olympus-global.com>, for information on Micro cantilevers.
- [16] M. Dukic, J. D. Adams, and Georg E. Fantner. “Piezoresistive AFM cantilevers surpassing standard optical beam deflection in low noise topography imaging.” *Scientific reports* 5 (2015): 16393.
- [17] J. D. Adams, B. W. Erickson, J. Grossenbacher, J. Brugger, A. Nievergelt, and G. E. Fantner. “Harnessing the damping properties of materials for high-speed atomic force microscopy.” *Nature nanotechnology* 11, no. 2 (2016): 147-151.
- [18] M. S. Rana, H. R. Pota, and I. R. Petersen. “Performance of sinusoidal scanning with MPC in AFM imaging.” *IEEE/ASME Transactions on Mechatronics* 20, no. 1 (2015): 73-83.
- [19] K. K. Leang, A. J. Fleming. “High-speed serial-kinematic SPM scanner: design and drive considerations.” *Asian journal of control* 11, no. 2 (2009): 144-153.
- [20] S. P. Wadikhaye, Y. K. Yong, B. Bhikkaji, and S. O. R. Moheimani. “Control of a piezoelectrically actuated high-speed serial-kinematic AFM nanopositioner.” *Smart Materials & Structures* 22, no. 2 (2014): 025030.
- [21] S. P. Wadikhaye, Y. K. Yong, and S. R. Moheimani. “Design of a compact serial-kinematic scanner for high-speed atomic force microscopy: An analytical approach.” *Micro & Nano Letters* 7, no. 4 (2012): 309-313.

- [22] S. P. Wadikhaye, Y. K. Yong and S. O. R. Moheimani. "A serial-kinematic nanopositioner for high-speed atomic force microscopy." *Review of Scientific Instruments* 85, no. 10 (2014): 105104.
- [23] B. J. Kenton, and K. K. Leang. "Design and control of a three-axis serial-kinematic high-bandwidth nanopositioner." *IEEE/ASME Transactions on Mechatronics* 17, no. 2 (2012): 356-369.
- [24] G. Schitter, P. J. Thurner, and P. K. Hansma. "Design and input-shaping control of a novel scanner for high-speed atomic force microscopy." *Mechatronics* 18, no. 5 (2008): 282-288.
- [25] C. Li, G. Gu, M. Yang, and L. Zhu. "Design, analysis and testing of a parallel-kinematic high-bandwidth XY nanopositioning stage." *Review of Scientific instruments* 84, no. 12 (2013): 125111.
- [26] S. O. Cisneros, J. L. D. V. Padilla, I. E. D. García, J. R. Dominguez, and J. J. Raygoza Panduro. "Design and implementation of a DC motor control using Field Programmable Analog Arrays." In *Electrical Engineering, Computing Science and Automatic Control (CCE), 2015 12th International Conference on*, pp. 1-6. IEEE, 2015.
- [27] D. A. Visan, I. Lita, and I. B. Cioc. "Temperature control system based on adaptive PID algorithm implemented in FPAA." In *Electronics Technology (ISSE), 2011 34th International Spring Seminar on*, pp. 501-504. IEEE, 2011.
- [28] S. P. Wadikhaye, B. Bhikkaji, S. R. Moheimani, and Y. K. Yong. "Analog implementation of a damping and tracking controller for a high-speed XY nanopositioner." In *American Control Conference (ACC), 2012*, pp. 3811-3816. IEEE, 2012.
- [29] Anadigm, see <http://www.anadigm.com>, for information on Anadigm FPAA.
- [30] R. C. Hibbeler. *Statics and mechanics of materials*. Pearson Higher Ed, 2013.
- [31] N. Lobontiu. *Compliant mechanisms: design of flexure hinges*. CRC press, 2002.
- [32] M. S. Rana, Hemanshu Roy Pota, and Ian R. Petersen. "Improvement in the Imaging Performance of Atomic Force Microscopy: A Survey." *IEEE Transactions on Automation Science and Engineering* 14, no. 2 (2017): 1265-1285.
- [33] Y. Liu, J. Shan, and U. Gabbert. "Feedback/feedforward control of hysteresis-compensated piezoelectric actuators for high-speed scanning applications." *Smart Materials and Structures* 24, no. 1 (2014): 015012.

- [34] G. Gu, L. Zhu, C. Su, H. Ding, and S. Fatikow. "Modeling and control of piezo-actuated nanopositioning stages: A survey." *IEEE Transactions on Automation Science and Engineering* 13, no. 1 (2016): 313-332.
- [35] D. Habineza, M. Rakotondrabe, and Y. Gorrec. "Bouc-Wen modeling and feedforward control of multivariable hysteresis in piezoelectric systems: application to a 3-DoF piezotube scanner." *IEEE Transactions on Control Systems Technology* 23, no. 5 (2015): 1797-1806.
- [36] Y. Liu, S. Tong, CL. P. Chen, and D. Li. "Neural controller design-based adaptive control for nonlinear MIMO systems with unknown hysteresis inputs." *IEEE transactions on cybernetics* 46, no. 1 (2016): 9-19.
- [37] K. Cai, Y. Tian, F. Wang, D. Zhang, X. Liu, and B. Shirinzadeh. "Modeling and tracking control of a novel XYθz stage." *Microsystem Technologies* (2017): 1-14.
- [38] K. Cai, Y. Tian, F. Wang, D. Zhang, X. Liu, and B. Shirinzadeh. "Design and control of a 6-degree-of-freedom precision positioning system." *Robotics and Computer-Integrated Manufacturing* 44 (2017): 77-96.